

# Suzaku and XMM-Newton Observations of Diffuse X-ray Emission from the Eastern Tip Region of the Carina Nebula

Yuichiro EZOE<sup>1</sup>, Kenji HAMAGUCHI<sup>2,3</sup>, Robert A. GRUENDL<sup>4</sup>, You-Hua CHU<sup>4</sup>,  
Robert PETRE<sup>5</sup>, and Michael F. CORCORAN<sup>2,3</sup>

<sup>1</sup> *Tokyo Metropolitan University, 1-1, Minami-Osawa, Hachioji, Tokyo, 192-0397, JAPAN*

<sup>2</sup> *CRESST and X-ray Astrophysics Laboratory NASA/GSFC, Greenbelt, MD 20771, USA*

<sup>3</sup> *Universities Space Research Association, 10211 Wincopin Circle, Suite 500, Columbia, MD 21044-3432, USA*

<sup>4</sup> *Department of Astrophysics, University of Illinois, Urbana, IL 61801, USA*

<sup>5</sup> *Astrophysics Science Division, NASA Goddard Space Flight Center, Greenbelt, MD 20771*  
*ezeoe@phys.metro-u.ac.jp*

(Received ; accepted )

## Abstract

The eastern tip region of the Carina Nebula was observed with the Suzaku XIS for 77 ks to conduct a high-precision spectral study of extended X-ray emission. XMM-Newton EPIC data of this region were also utilized to detect point sources. The XIS detected strong extended X-ray emission from the entire field-of-view with a 0.2–5 keV flux of  $0.7 \sim 4 \times 10^{-14}$  erg s<sup>-1</sup> arcmin<sup>-2</sup>. The emission has a blob-like structure that coincides with an ionized gas filament observed in mid-infrared images. Contributions of astrophysical backgrounds and the detected point sources were insignificant. Thus the emission is diffuse in nature. The X-ray spectrum of the diffuse emission was represented by a two-temperature plasma model with temperatures of 0.3 and 0.6 keV and an absorption column density of  $2 \times 10^{21}$  cm<sup>-1</sup>. The X-ray emission showed normal nitrogen-to-oxygen abundance ratios and a high iron-to-oxygen abundance ratio. The spectrally deduced parameters, such as temperatures and column densities, are common to the diffuse X-ray emission near  $\eta$  Car. Thus, the diffuse X-ray emission in these two fields may have the same origin. The spectral fitting results are discussed to constrain the origin in the context of stellar winds and supernovae.

**Key words:** X-ray: ISM — ISM: abundances — ISM: individual (Carina nebula) — stars: winds — stars: supernovae: general

## 1. Introduction

Diffuse X-ray emission extending over several to tens pc has been reported in many massive star-forming regions, such as NGC 2024 (Ezoe et al. 2006a), the Orion Nebula (Güedel et al. 2008), the Rosette Nebula, (Towneley et al. 2003), M17 (Towneley et al. 2003; Hyodo et al. 2008), RCW 38 (Wolk et al. 2002), NGC 6334 (Ezoe et al. 2006b), the Carina Nebula (Hamaguchi et al. 2007), W49 (Tsujimoto et al. 2006), NGC 3603 (Moffat et al. 2002), the Arches Cluster (Yusef-Zadeh et al. 2002; Tsujimoto et al. 2007), and the Quintuplet Cluster (Wang et al. 2002). This diffuse component contributes a considerable fraction of the total X-ray emission and shows different spectral characteristics among these regions. Diffuse X-ray emission can be roughly classified into three types: thin-thermal plasma emission with a temperature  $kT \sim 0.1\text{--}1$  keV, higher-temperature plasma emission with  $kT \sim 2\text{--}10$  keV, and possibly non-thermal emission with a photon index of 1-1.5. These phenomena can be explained by plasma heating and particle acceleration in strong shocks by fast stellar winds from young OB stars (Towneley et al. 2003; Ezoe et al. 2006a; Ezoe et al. 2006b; Güedel et al. 2008) and/or past supernova remnants (SNRs) (Wolk et al. 2002; Hamaguchi et al. 2007). The precise origin of diffuse X-ray emission, however, is often unclear.

Recently Hamaguchi et al. (2007) suggest that the origin of diffuse X-ray emission can be constrained by plasma diagnostics or measurements of elemental abundances. While main-sequence late-O to early B stars have nearly solar abundances (e.g., Cunha et al. 1994; Daflon et al. 2004), evolved stars show non-solar elemental compositions due to the CNO cycle. For instance, the plasma will be overabundant in nitrogen if its origin is the wind from a nitrogen-rich Wolf-Rayet star. On the other hand, the plasma will be overabundant in oxygen, neon, and silicon if it is produced by a Type II SNR (e.g., Tsujimoto et al. 1995). The low-temperature ( $kT \sim 0.1\text{--}1$  keV) type of diffuse X-ray emission is ideal for such diagnostic studies, because a variety of K-shell lines exist in the 0.2–2 keV range.

The Carina Nebula is an excellent site to investigate plasma diagnostics of diffuse X-ray emission. At a distance of 2.3 kpc, it is one of the most active massive star forming regions in the Galaxy. It contains eight massive stellar clusters: Trumpler 14, 15, 16, Collinder 228, Bochum 10, 11, NGC 3293, and NGC 3324. In total, there exist more than 64 O stars (Feinstein 1995; Smith et al. 2006), including the extreme-type luminous blue variable  $\eta$  Car and four Wolf-Rayet stars. The age of the nebula is estimated to be  $\sim 3$  Myr based on the most evolved stars and the size of the HII region (Smith et al. 2000). The young massive stars that are still enshrouded in gas and dust have been observed in optical, infrared, and radio wavelengths (e.g., Harvey et al. 1979; Smith et al. 2000; Yonekura et al. 2005). The number counts of the most massive O stars, e.g., O3 stars, suggest that the star-formation activity of the Carina Nebula rivals those of the most active regions, such as NGC 3603 at  $D = 6.9$  kpc and W49 at  $D = 11.4$  kpc. The proximity of the Carina Nebula, compared with NGC 3603

and W49, makes it the best target to study diffuse X-ray emission resulting from star-forming activities.

Seward et al. (1979) first suggested the existence of possible diffuse soft X-ray emission in the Carina Nebula with a luminosity of  $\sim 10^{35}$  erg s $^{-1}$  and a spatial extent of several pc, using Einstein observations. Although the limited energy and spatial resolution of Einstein hindered the determination of precise plasma parameters and the contribution from point sources, Seward & Chebowski (1982) postulated that the extended X-rays were from hot gas with  $T \sim 10^7$  K. With Chandra, Evans et al. (2003) confirmed the existence of diffuse X-ray emission near  $\eta$  Car in addition to point sources; however, the limited photon statistics and high background prevented detailed spectral analysis. Hamaguchi et al. (2007) obtained spectra of the diffuse X-ray emission around  $\eta$  Car with Suzaku. Owing to the good low-energy response and the low background of the X-ray CCD onboard Suzaku, the spectra extracted from the regions north and south of  $\eta$  Car can be modeled with high precision; both spectra are best represented by three-temperature plasma models with  $kT \sim 0.2$ ,  $\sim 0.6$ , and  $\sim 5$  keV. Analyzing the Suzaku data in conjunction with XMM-Newton and Chandra data, Hamaguchi et al. (2007) concluded that the 0.2 keV and 0.6 keV components most likely originated from diffuse plasma, but the 5 keV component could not be easily distinguished from the unresolved point sources. They found that the iron and silicon abundances were significantly different in the north and south regions, and that the nitrogen-to-oxygen abundance ratios in both regions were far lower than those of stellar winds from evolved massive stars such as  $\eta$  Car and WR25 in this field. From these results, they concluded that the diffuse X-ray emission near  $\eta$  Car originated from one or multiple SNRs.

We have studied extended X-ray emission from an eastern tip region of the Carina Nebula. Located  $\sim 30'$  ( $\sim 20$  pc) from  $\eta$  Car, this region is less contaminated by X-ray emission from OB stars than the regions near  $\eta$  Car. Previous Einstein observations have revealed strong extended X-ray emission in this region, although no massive stars earlier than B3 are known here (Seward & Chebowski 1982). It is not known whether this emission is truly diffuse and, if so, whether its origin is similar to that of the regions near  $\eta$  Car. In this paper we report the first detailed spectral analysis of the extended X-ray emission in this eastern tip region of the Carina Nebula using Suzaku observation. To augment the limited angular resolution of Suzaku, the analysis also made use of XMM-Newton data.

## 2. Suzaku Observation

Suzaku is the 5th Japanese X-ray observatory (Mitsuda et al. 2007). It carries four scientific instruments; X-ray optics or the X-Ray Telescope (XRT: Serlemitsos et al. 2007); an X-ray calorimeter (XRS: Kelly et al. 2007); four X-ray CCDs (XIS: Koyama et al. 2007); and a hard X-ray detector (HXD: Takahashi et al. 2007; Kokubun et al. 2007). The XIS consists of three front-illuminated (FI) CCDs (XIS0, 2, and 3) and one back-illuminated (BI) CCD (XIS1).

Due to the low-earth orbit of Suzaku and the large effective area, the XIS has the lowest particle backgrounds among all X-ray CCDs in currently available X-ray observatories. Furthermore, the XIS has good energy resolution and superior low-energy response with negligible low-energy tails, compared to the other X-ray CCDs onboard XMM-Newton and Chandra.

We observed the eastern tip region of the Carina Nebula with Suzaku on 2006 June 5. During the observation, the XIS and HXD were operated in the normal mode. In the present paper, we use only the XIS data because we are interested in the spectral analysis of the soft extended X-ray emission.

The data reduction was performed on the version 1.2.2.3 screened data provided by the Suzaku processing facility, using the HEASoft analysis package ver 6.1.1. No background flares were seen in the data. The net exposure of each FI and BI chip was 77 ks. For spectral fits, we generated response matrices and auxiliary files with `xisrmfgen` and `xissimarfgen` released on 2006 October 26. The in-flight gradual degradation of energy resolution and absorption due to XIS contamination were considered in these softwares.

### 3. Extended X-ray Emission

Figure 1a shows the location of our observation (top left box) on an MSX 8.28  $\mu\text{m}$  image of the Carina Nebula retrieved from the NASA/IPAC Infrared Science Archive <sup>1</sup>. This mid-IR image is dominated by cationic polycyclic aromatic hydrocarbon emission in photodissociation regions (Smith et al. 2000) and traces the surface of molecular clouds that are ionized by stellar winds and ultra-violet radiations from OB stars. A curved mid-infrared filament runs across the XIS field-of-view (FOV). Figure 1b shows an X-ray overview of the same area with XMM-Newton MOS<sup>2</sup>. In X-rays, there exists patchy extended soft X-ray emission whose distribution roughly follows the mid-infrared filament. This suggests that the X-ray emission contributes to the ionization of the molecular cloud and that the emitting hot gas is in contact with the surface of the molecular clouds.

We created Suzaku XIS images in 0.2–2 and 2–10 keV bands, as shown in figure 2. The vignetting in the images has been corrected by dividing the observed images by model XIS images produced with the XRT+XIS simulator `xissim` for a uniform surface brightness. In simulations, we assumed monochromatic X-rays of energy 1.49 keV and 8.05 keV, since the vignetting is best studied in these energies (Serlemitsos et al. 2007). A blob-like extended X-ray emission is clearly detected in the soft X-ray band. No significant X-ray emission is seen in the hard X-ray band, which is consistent with the XMM-Newton image (figure 1 b).

To evaluate the significance of the extended X-ray emission, we defined a region named blob, as shown in figure 2. The total area of the blob region is 234 arcmin<sup>2</sup>, or 105 pc<sup>2</sup>. We

---

<sup>1</sup> <http://irsa.ipac.caltech.edu/applications/MSX/MSX/>

<sup>2</sup> [http://xmm.esac.esa.int/external/xmm\\_science/gallery/](http://xmm.esac.esa.int/external/xmm_science/gallery/)

extracted the XIS0-3 spectra from this region. To evaluate the background, we utilized spectra accumulated from observations of the night side of the Earth, as the night Earth backgrounds reproduced well all the observed spectra above  $\sim 6$  keV, where the instrumental background dominated. The background-subtracted XIS1 (BI) and XIS0 + 2 + 3 (FI) spectra are shown in figure 3a, and their 0.2–5 keV count rates with  $1\sigma$  uncertainties are  $1.073 \pm 0.004$  (BI) and  $0.609 \pm 0.002$  (FI) counts  $s^{-1}$ , respectively. The emission is highly significant and shows a number of emission lines such as O VII, O VIII, Ne IX, Ne X, Mg XI, Si XIII, and S XV. Lines from these ions in different ionization states, such as O VII and Si XIII, suggest that the extended X-rays are from not a single-temperature but multi-temperature plasma.

We extracted spectra from two surrounding regions named east and nw, as shown in figure 2. The areas of the east and nw regions are  $47 \text{ arcmin}^2$  (or  $21 \text{ pc}^2$ ) and  $21 \text{ arcmin}^2$  (or  $9.3 \text{ pc}^2$ ), respectively. We again used the night Earth spectra at the respective detector positions as backgrounds. The background-subtracted spectra are shown in figures 3b and c. Although their surface brightnesses are an order-of-magnitude lower than that in the blob region, there exist signs of emission lines from O VII, Ne IX, Ne X, Mg XI, and Si XIII. Thus extended X-ray emission appears to be present over the entire FOV. The surface brightness below 0.3 keV and above 2 keV is similar in all three regions. Therefore, in addition to the plasma emission that is dominant between 0.3 and 2 keV, there must be additional X-ray sources. Plausible candidates are the local hot bubble (LHB), the cosmic X-ray background (CXB), the galactic ridge X-ray emission (GRXE), and point sources. LHB and CXB are uniform and common background sources existing in all X-ray observations. GRXE is also a uniform X-ray background and must contribute to the emission because the observational FOV is located in the Galactic plane ( $l = 288^\circ$ ,  $b = -0^\circ.4$ , see figure 1a). The point sources, on the other hand, are position-dependent. Contamination from these astrophysical backgrounds and point sources needs to be carefully considered in order to characterize the possible diffuse emission from the Carina Nebula.

#### 4. Point Sources

To quantify the contribution from point sources, we analyzed the XMM-Newton data. XMM-Newton observed this region on 2004 December 7 for 27 ks. The European Photon Imaging Camera (EPIC) provided CCD imaging spectroscopy with one pn camera (Strüder et al. 2001) and two MOS cameras (Turner et al. 2001). The medium optical blocking filter was used. As shown in figure 1b, the FOVs of MOS cover the entire FOV of the XIS. We analyzed the archival processed data using SAS (Science Analysis Software) version 7.0.0, following the SAS user’s guide<sup>3</sup>. The event files were time-filtered to exclude periods of high background, during which the count rate from the entire CCD area at energies  $>10$  keV is more than 1.2

---

<sup>3</sup> [http://xmm.esac.esa.int/external/xmm\\_user\\_support/documentation/sas\\_usg/USG/](http://xmm.esac.esa.int/external/xmm_user_support/documentation/sas_usg/USG/)

times the average rate for each MOS and pn observation. This removed  $\sim 1$  ks from each observation, and yielded 22 and 26 ksec of usable exposure for pn and each MOS, respectively. Source detection was accomplished with the SAS program `edetect_chain`. Images in 8 bands (0.2–0.5, 0.5–2.0, 2.0–4.5, 4.5–7.5, 7.5–12.0, and 0.2–12.0 keV) were utilized, in order not to miss very soft or very hard sources. The resulting source list was checked manually for spurious detections and missed sources. As a result, 10 sources have been detected, among which 5 sources were within the FOV of the XIS. The locations of these X-ray point sources are marked by circles in figure 1b.

For each individual point source, we extracted counts using a circular region of a 30 arcsec radius centered at the source. Background counts were extracted from an adjacent annular region with an outer radius of 1 arcmin. In the case that the annular region included other sources, the background was then extracted from a nearby circular source-free region. To identify counterparts of these X-ray point sources in other wavelengths, we searched the  $2\mu\text{m}$  all sky survey catalog (2MASS)<sup>4</sup> and the AXAF Guide and Acquisition Star Catalog (AGAST)<sup>5</sup> for candidates within 10 arcsec, the angular resolution of XMM-Newton. In cases where multiple candidates exist, we chose the closest one as the most plausible counterpart. Among the 10 X-ray sources, 9 have counterparts in 2MASS and 1 has a counterpart in AGAST. The properties of these individual sources are summarized in table 1.

We examined the 10 sources for possible temporal variations. For each source, we produced pn and MOS X-ray light curves in the 0.4–10 keV band using a binning size of 512 s bin<sup>-1</sup>. The light curves were examined against a constant hypothesis in terms of  $\chi^2$  statistics. If the  $\chi^2$  probability of constancy became less than 4%, at least in one detector, we regarded the source as variable. Only the source No.3 has been found to be variable. It showed a factor of about 5 increase in the first 5 ks of the observation, decreased in the next 5 ks, and stayed constant in the rest. Such rapid temporal variations strongly suggest that No.3 is a young low-mass star.

We also conducted spectral analysis for 4 bright sources (No.1, 2, 4, and 7) that had  $> 100$  counts in the pn observation. We analyzed only the pn spectra because of the limited statistics of MOS. The SAS tasks `rmfgen` and `arfgen` were utilized to generate response matrix files and auxiliary files for each source. We fitted the spectra using a thin-thermal plasma emission model in collisional equilibrium (the APEC mode; Smith et al. 2001) convolved with the interstellar absorption. Such models, with abundances fixed at 0.3 solar, are commonly used in X-ray spectral analyses of star-forming regions (e.g., Getman et al. 2005). We found that all the spectra except that of No.1 were well represented by this simple model. For the No.1 spectrum, we tried a two-temperature plasma emission model with a common absorption, and were able to find acceptable fits. The fitting results are summarized in table 2 and figure

---

<sup>4</sup> <http://irsa.ipac.caltech.edu/index.html>

<sup>5</sup> <http://cxc.harvard.edu/cgi-gen/cda/agasc/agascInterface.pl>

4.

Source No.1 has a very hard continuum without any sign of emission lines, thus it may be a background active galactic nucleus. Source No.2 may be an embedded young low-mass star because it has a large absorption column density and a moderate temperature, while source No.4 may be a foreground star because of its small absorption column and moderate temperature. Source No.7 is peculiar with a low temperature and possibly high luminosity. Its position is within 8 arcsec from the X-ray source No.78 in an XMM-Newton observation of  $\eta$  Car reported by Colombo et al. (2003). Further optical spectroscopic study is needed to identify the nature of this source.

We estimated X-ray fluxes of the other 6 sources assuming a thin-thermal plasma model and convolving it with an estimated interstellar absorption of  $N_{\text{H}} = 1.3 \times 10^{22} \text{ cm}^{-2}$ . We adopted a temperature of 3 keV and a metal abundance of 0.3 solar that are typical of emission from young stars (e.g., Imanishi et al. 2001). WebPIMMS<sup>6</sup> was used to convert the pn count rates to X-ray fluxes. The results are shown in table 1. The fluxes range from  $2 \times 10^{-14}$  to  $4 \times 10^{-13} \text{ erg s}^{-1} \text{ cm}^{-2}$ .

## 5. Contamination from Astrophysical Backgrounds and Point Sources

We proceeded to estimate contribution to the observed X-ray emission by LHB, CXB, GRXE, and point sources. For the LHB, CXB, and GRXE, we assumed the same models in Hamaguchi et al. (2007): the Raymond-Smith thin-thermal plasma model with  $kT \sim 0.1 \text{ keV}$  and a surface brightness of  $\sim 4 \times 10^4 \text{ counts s}^{-1} \text{ arcmin}^{-2}$  for LHB based on Snowden et al. (1998), the model Id1 in table 2 of Miyaji et al. (1998) for CXB, and the free abundance model in table 8 of Ebisawa et al. (2005) with the X-ray flux of  $1.4 \times 10^{-11} \text{ erg cm}^{-2} \text{ s}^{-1} \text{ deg}^{-2}$  (3–20 keV) for GRXE. We used the same spectral parameters except for the normalization to fit, which was adjusted. To estimate the X-ray fluxes from these components with different spatial distribution, we prepared an arf file for the uniform emission (LHB, CXB, and GRXE) by using the `xissimarfgen` program, while we created an arf file for each point source. We used the best-fit models in table 2 for the bright point sources and assumed the typical spectral model of young low-mass stars for the other faint point sources ( $kT = 3 \text{ keV}$  and  $N_{\text{H}} = 1.3 \times 10^{22} \text{ cm}^{-2}$ ) using the APEC emission code.

In figure 5a, we plot the estimated contamination from LHB, CXB, GRXE, and point sources in the blob region. Below 0.3 keV, LHB accounts for the X-ray emission, while X-rays above 2 keV can be explained by the sum of CXB, GRXE and point sources. This makes a sharp contrast to the  $\eta$  Car region where a residual hard X-ray emission is seen above 2 keV. The excellent fit of these sources to the spectrum below 0.3 keV and above 2 keV supports the validity of our estimation. Thus, almost all the excess counts in 0.3–2 keV can be considered

---

<sup>6</sup> <http://heasarc.gsfc.nasa.gov/Tools/w3pimms.html>

to be truly diffuse plasma emission. This conclusion is also supported by the clear spectral differences between the diffuse plasma and point sources.

In the same way, we estimated the X-ray contamination in the east and nw regions as shown in figures 5b and c. In both regions, LHB, CXB, GRXE, and point sources explain all the emission in  $< 0.3$  and  $> 2$  keV as well as in the blob region, but there are still excesses in 0.3–2 keV. Therefore, diffuse soft X-ray emission exists in these fields, too.

## 6. Spectral Analysis

### 6.1. The blob Region

The nature of the diffuse X-ray emission is investigated through spectral analysis. We simultaneously fitted the 0.2–5 keV XIS BI and FI spectra of the blob region. We created XIS arf files using `xissimarfgen`, assuming the 0.4–2 keV XMM MOS image in figure 1b as spatial distribution of the diffuse X-ray emission. In single or two-temperature plasma models utilized below, we allow the abundances of the noticeable elements (O, Ne, Mg, Si, S, and Fe) to vary, while those of the other elements were fixed at 0.3 solar value, which is generally seen in low-resolution CCD spectra of young stars.

In addition to the plasma model for the diffuse X-ray emission, we introduced a thin-thermal plasma model and a power-law model to reproduce the LHB, CXB, GRXE, and point source contributions (§5). For the plasma model of LHB, we fixed the temperature at 0.1 keV and the abundances at 1 solar, but allowed the normalization to vary. For simplicity, the CXB, GRXE, and point sources were together approximated by a single power-law model with the photon index fixed at 1.5 and convolved with the same absorption of the diffuse X-ray emission. To take into account possible uncertainties in the energy scale calibration, we introduced two additional fitting parameters, gain and offset. Throughout the fittings below, the best-fit energy scale and offset values were  $< 1$  % and  $< 6$  eV, respectively, consistent with the current calibration uncertainties <sup>7</sup>.

We first tested a single-temperature thin-thermal plasma model convolved with an absorption. This simple model yielded an unacceptable best fit for the spectra with  $\chi^2/\text{d.o.f.}$  of 2.4. The best-fit temperature,  $kT = 0.59$  keV, was too high to reproduce the significant OVII and NeIX lines. We then tried a commonly-absorbed two-temperature plasma model as shown in figure 6a and table 3 (model 1). This model represents the data far better ( $\chi^2/\text{d.o.f.}$  of 1.2). A small discrepancy of the fit to the data at 0.5–0.8 keV and 1.1–1.2 keV may be caused by inaccuracy of the Fe L-shell emission line model and calibration uncertainty near the mirror Au L edges, respectively. Indeed, similar discrepancies at 0.5–0.8 keV can be seen in other Suzaku XIS spectral fits (e.g., Hamaguchi et al. 2007). Therefore, we think the best-fit two-temperature model represents the data well, although the  $\chi^2$  is still not above the 90% confidence level.

---

<sup>7</sup> <http://www.astro.isas.jaxa.jp/suzaku/process/caveats/>

## 6.2. The east and nw Regions

Similar to the analysis of the blob region, we fitted the east and nw spectra with a two-temperature plasma model. Since no evident spatial structures were seen in these regions (figure 2), we created arf files assuming a uniform emission. We did not use the additional fitting parameters gain and offset because the photon statistics were limited. The results are shown in figures 6b and c, and table 3. In both regions, the fits are acceptable and all resulting parameters except the surface brightness are consistent with those in the blob region, although the uncertainties are large. As expected from figure 2, the surface brightness of the east and nw regions is a factor of  $\sim 5$  lower than that in the blob region.

We also tried a single-temperature plasma model and obtained acceptable fits in both regions, but the best-fit column densities were small,  $\sim 8 \times 10^{20} \text{ cm}^{-2}$ , and the best-fit temperatures were high,  $\sim 0.6 \text{ keV}$ . Such a large variation in the column density within the XIS FOV is inconsistent with the CO map (figure 1a), although the CO gas can lie behind the X-ray emitting gas. There is also a hint of OVII K emission in both spectra (figures 3 b and c) that cannot be reproduced by this best-fit single-temperature model. Therefore, it is likely that the east and nw spectra are also best fitted by a two-temperature plasma model.

## 6.3. XMM-Newton spectra

We also analyzed the XMM-Newton observations of the blob region with the same data used in the point source analysis (§4). We used only the MOS data with relatively low particle background events, whose background spectrum during the observation can be easily estimated from the ESAS package<sup>8</sup>. We used SAS version 7.0.0 and ESAS version 1.0 for the analysis, and generated response matrices using the `rmfgen` and `arfgen`. We found that the two-temperature plasma model well represents the MOS spectra, as was the case for the Suzaku XIS spectra. Figure 7 and table 5 show the fitting result. Since there can be C  $K_\alpha$  emission around 0.4 keV, we allowed the C abundance to vary. The energy band of 1.16–1.28, 1.4–1.6, and 1.7–1.8 keV are omitted in order to exclude the instrumental emission lines from Mg  $K_\alpha$ , Al  $K_\alpha$ , and Si  $K_\alpha$ . Because the low energy tail of the MOS response prevents the distinction between the diffuse low temperature plasma component and the LHB, only an upper limit is obtained for the LHB. Alternatively the best-fit column density becomes somewhat lower than that in table 3 (model 1), to compensate the decreased low energy counts by the LHB component. The other two-temperature plasma parameters such as temperatures and abundances are surprisingly similar to those in table 3 (model 1). The only difference is the higher power-law component flux. This may be caused by the relatively higher background of XMM-Newton observations and their higher uncertainty. We thus conclude that the XIS and MOS data are consistent with each other and the fitting result of the XIS data is reliable.

---

<sup>8</sup> [http://heasarc.gsfc.nasa.gov/docs/xmm/xmmhp\\_xmmesas.html](http://heasarc.gsfc.nasa.gov/docs/xmm/xmmhp_xmmesas.html)

## 7. Discussion

We investigated extended X-ray emission in the eastern tip region of the Carina Nebula with Suzaku XIS. For the first time, we conducted detailed spectral analysis of the X-ray emission and found that there is indeed diffuse X-ray emission, even considering LHB, CXB, GRXE, and point sources. The diffuse X-ray emission is well represented by a two-temperature plasma model with  $kT \sim 0.25$  and  $\sim 0.55$  keV. Emission measures and abundances of O, Ne, Mg, Si, S, and Fe are well constrained owing to the good photon statistics and the excellent energy response of XIS. Below we estimate plasma properties based on the spectral fitting and then compare the spectral parameters such as absorption column density, temperature and abundance to those in the  $\eta$  Car region, in order to assess the origin of the diffuse plasma.

### 7.1. Physical Properties of the Plasmas

High signal-to-noise XIS spectra enable us to accurately constrain the parameters of the diffuse plasma in the eastern tip region of the Carina Nebula. The best-fit column density of  $N_{\text{H}} \sim 2\text{--}3 \times 10^{21} \text{ cm}^{-2}$  and also the temperatures of  $kT \sim 0.2\text{--}0.3$  keV and  $0.4\text{--}0.6$  keV in the blob, east and nw regions agree very well with those in the  $\eta$  Car regions (see the medium-temperature components of the  $N_{\text{H}}$ ,  $kT$  tied model in table 2 of Hamaguchi et al. 2007 or hereafter H2007 model;  $N_{\text{H}} \sim 2 \times 10^{21} \text{ cm}^{-2}$ ,  $kT \sim 0.2$  keV and  $0.6$  keV). Although the high-temperature component represented by a hot plasma model with  $kT \sim 5$  keV in the H2007 model is not seen in the eastern tip region, this is thought to be a composite of diffuse hard X-ray emission and contaminations from CXB, GRXE, and point source, and hence can be ignored. This similarity in basic plasma parameters provides strong evidence that the diffuse plasma in the vicinity of the Carina Nebula has the same origin.

The continuous distribution of the diffuse X-ray emission over the Carina Nebula, as shown in figure 1, supports this hypothesis. Thus, we can draw a scenario that the X-ray emitting diffuse plasma generated by stellar winds from OB stars and/or SNRs forms hot bubbles with the size of several tens of pc and ionizes ambient molecular clouds which can be seen in the mid-infrared emission.

To investigate the origin of the diffuse plasma, we estimate physical properties of the plasma in the blob region. We assume that the plasma in the blob region have a prolate ellipsoidal shape with the major and minor axis lengths of 8 and 3 pc, respectively. Following the plasma analysis by Townsley et al. (2003), we estimate the electron density, the pressure, the total energy content, the cooling time and the mass of the plasma from the observed X-ray luminosity, temperatures, and the assumed volume. We derived two sets of plasma parameters for the two-temperature components from model 1 in table 3. The derived parameters are summarized in table 6. Below we examine the two interpretations, i.e., stellar winds from OB stars and SNRs, based on these derived parameters. Because there are no massive OB stars in the eastern tip region, we must consider the massive stellar clusters in the central part of the

Carina Nebula for the former scenario.

The estimated plasma pressure  $P$  is on the order of  $\sim 10^6$  K cm $^{-3}$  and should be larger than that of the surrounding gas in the eastern tip region since both the CO and radio continuum intensities are weak in the vicinity of the blob region (Yonekura et al. 2005; Huchtmeier & Day 1975). This means that diffuse plasma in the eastern tip region could flow from its neighbor. If we consider that the plasma originated in stellar winds from OB stars near  $\eta$  Car and has been propagated to this region at the plasma sound velocity, the crossing time will be 0.1 Myr. Because this time scale is much shorter than that of the radiative cooling timescale,  $t_{\text{cool}} > 1$  Myr, the plasma temperatures can be held constant. OB stars are able to continuously produce the plasma during 0.1 Myr since their typical life time is at least ten times longer. The SNR interpretation is also possible in terms of the pressure if one or multiple SNRs occurred in these regions.

The total thermal energy of the plasma,  $U = 1 \times 10^{48}$  ergs, is marginally lower than the total kinetic energy supplied by the stellar wind from a single massive star within  $\sim 1$  Myr,  $\sim 3 \times 10^{48}$  ergs (Ezoe et al. 2006a). As the Carina Nebula contains  $> 64$  OB stars, the observed thermal energy can be easily supplied by the mechanical energy of the stellar winds from the  $> 64$  OB stars,  $> 2 \times 10^{50}$  ergs. If all the diffuse X-ray emission observed with Einstein has the same origin, the total plasma energy will be about 10 times larger, i.e.,  $1 \times 10^{49}$  ergs. Assuming that the stellar winds from these  $> 64$  OB stars ( $> 2 \times 10^{50}$  ergs) are responsible for the hot plasma, the kinetic-to-thermal energy conversion efficiency will be  $< 5\%$ . According to Weaver et al. (1977), the thermal energy in the shocked stellar wind is 5/11 of the total stellar wind kinetic energy. Thus, this conversion efficiency may be doubled,  $< 10\%$ , which is comparable to that in M17 ( $\sim 10\%$ , Townsley et al. 2003) and larger than that in the Orion nebula ( $\sim 0.01\%$ , Güedel et al. 2008). In the SNR case, we can also explain the energy by only one canonical supernova ( $\sim 1 \times 10^{51}$  ergs) even if we must explain all the diffuse X-ray emission in the entire Carina Nebula.

The mass of the plasma,  $M_{\text{plasma}} \sim 0.4M_{\odot}$ , needs at least four typical OB stars assuming a typical mass loss rate of stellar winds of  $10^{-7}M_{\odot}\text{yr}^{-1}$  in 1 Myr. If we consider the whole Carina Nebula, about  $> 80$  OB stars are necessary for the entire diffuse plasma mass. The known number of OB stars is thus marginal. On the other hand, one SNR again can supply this mass (e.g., Willingale et al. 2003).

Therefore, although both the stellar-wind and SNR interpretations are possible, SNR(s) can explain the derived plasma parameters such as the total plasma energy and the plasma mass, more easily. As suggested by Hamaguchi et al. (2007), the existence of the Carina flare supershell (Fukui et al. 1999) validates the SNR scenario. If true, the observed plasma temperatures of 0.3 and 0.6 keV limit the SNR age to less than  $\sim 10^4$  yr, since an older SNR would be in the radiative phase and efficiently cool down to less than 0.1 keV.

## 7.2. Abundance

The abundance pattern of the X-ray emitting plasma provides another key piece of information to constrain its origin. We showed abundance patterns of the blob region and that of the  $\eta$  Car regions in figures 8 a and b, respectively. Since Hamaguchi et al. (2007) divided the  $\eta$  Car region into the north and south regions and fitted the two spectra simultaneously with tied column density and temperatures in the H2007 model, two sets of abundances are shown.

All the metal abundances in the blob region (model 1, black) are significantly higher than those in the  $\eta$  Car regions. This may strengthen the result of Hamaguchi et al. (2007) that the metal abundances of the diffuse X-ray emission show spatial variations. However, there is a possibility that the fixed abundances of C, N, Al, Ar, Ca and Ni in table 3 influence the other metal abundances. Thus, we refitted the blob region spectra with different fixed abundance sets.

Firstly we tested one solar for the fixed abundances. In model 1, we implicitly assumed 0.3 solar for them because the value is generally used for young stars in star-forming regions. However, since any mixing of the plasma generated by either stellar winds or SNR(s) interacting with the ambient molecular clouds contains processed stellar material and may have higher abundances, it is thus worth considering the solar abundances in modeling the diffuse emission. The results are summarized in figure 8 a and table 3 (model 2). The  $\chi^2$  was comparable to that of model 1 and all the abundances increased by a factor of  $\sim 2$ , while the emission measures of the two plasma components decreased by about the same amount, to balance the increased line intensities. Since the SNRs with an age around  $10^4$  yrs, like the Cygnus Loop or Vela, globally show no strong deviation from solar abundances (McEntaffer & Cash 2008), this fitting result allows the SNR interpretation.

Next we assumed the abundances of the H2007 model in which all the abundances were allowed to vary and constrained with good photon statistics. We used two sets of fixed abundances corresponding to the north and the south fits. The results are summarized in figure 8 a and table 3 (models 3 and 4). In both cases, the fittings were acceptable and all the free abundances were significantly decreased. These changes were caused by the decreased N and Ni fixed abundances that influence the others via the NV K and Ni L emission lines. For instance, when we used the abundances for the north region (model 3), the N abundance changes from 0.3 to 0 solar and to compensate for the decreased photon counts in the 0.5–0.6 keV band, the normalization of the lower-temperature component ( $kT \sim 0.25$  keV) increases and the abundances of the other elements are suppressed. When the abundances for the south region (model 4) are utilized, the Ni L lines in the 0.8–1.4 keV range increases and the abundances of the other elements related to this energy band decreases. The abundances of the blob region approaches to those of the  $\eta$  Car region (figure 8 b) if we use these abundance sets.

The abundance values are therefore strongly influenced by the fixed abundances. In

model 2, all the abundances are around one solar, while in model 1, 3 and 4, the best-fit metal abundances are far less than one. This is due to the fact that the metal abundance and emission measure are coupled with each other. To decouple these parameters, we need more precise spectral measurements with X-ray microcalorimeters in future missions.

In spite of the difficulty to determine the absolute abundances, abundance patterns of the blob region in models 1-4 are similar to those in the  $\eta$  Car regions. This similarity is another line of evidence that the diffuse X-ray emission in the eastern tip region and the  $\eta$  Car region has the same origin.

Because the abundance patterns are rather independent of the fixed abundances, we can also evaluate the abundance ratio of different elements. Importantly, there is no significant overabundance in nitrogen to oxygen that is expected from the optical, UV and X-ray spectroscopy of  $\eta$  Car and WR 25 (Davidson et al. 1982; van der Hucht et al. 1981; Tsuboi et al. 1997). This result agrees with that in the  $\eta$  Car region (Hamaguchi et al. 2007) and suggests that, if stellar winds produced the diffuse X-ray plasma, the main drivers of the winds are main-sequence OB stars, and not evolved massive stars. Also the observed Fe/O ratio of 1.3–1.9 is too high compared to that of a type-II supernova, 0.5 (Tsujimoto et al. 1995). Although the Fe/O ratio increases up to 1 in type-II SNRs for less massive stars ( $\sim 13M_{\odot}$ , table 1 in Tsujimoto et al. 1995), this contradicts the fact that the more massive stars evolve faster and explode earlier.

We note that similar situations exist in other massive star forming regions. For example, detailed spectral study of the diffuse X-ray emission has been conducted with Suzaku in M17 (Hyodo et al. 2008). We plot the abundance pattern of the diffuse plasma in M17 in figure 8 c. As is the case for the Carina Nebula, it shows a high Fe/O ratio and not enhanced N-to-O ratio, the latter of which may be natural because M17 contains no WR stars (Townsend et al. 2003). Its subsolar abundances may be affected by the fixed values at 0.3 solar.

Thus, both the stellar-wind and SNR interpretations are possible in terms of the absolute abundances. The abundance pattern may favor plasma heating by winds from main-sequence OB stars. Another possibility is a mixture of stellar winds and SNRs. Also, since hot shocked gas by stellar winds and/or SNRs mix up interstellar gas, we may only see the interstellar abundances rather than stellar and/or SNR abundances. Further studies are necessary from both observational and theoretical aspects.

### 7.3. *Hard X-ray component*

The X-ray spectrum above 2 keV can be explained by contribution of CXB, GRXE and known point sources. This means that the residual hard X-ray emission, seen around  $\eta$  Carinae (Hamaguchi et al. 2007), localizes within  $\sim 30'$  from  $\eta$  Car. The scale size is consistent with an apparently extended hard X-ray emission discovered with the GINGA satellite (Koyama et al. 1990) though the GINGA result did not count out emission from known point sources. Because

soft ( $<2$  keV) diffuse X-ray spectra of the eastern tip region and the southern part of the  $\eta$  Car region are almost identical, the diffuse plasma would not relate to the residual hard X-ray emission. Probably, the residual emission originates from a large number of low mass young stars embedded in the cloud around  $\eta$  Car, which are too faint to be detected individually.

## 8. Conclusion

In the present paper, we have investigated the properties of diffuse X-ray emission associated with the eastern tip region of the Carina Nebula using the Suzaku and XMM-Newton data. Our conclusion is as follows.

(1) Strong extended X-ray emission was detected from the entire field-of-view of Suzaku with a 0.2–5 keV surface brightness of  $0.7\sim 4\times 10^{-14}$  erg s $^{-1}$  arcmin $^{-2}$ . Comparisons with the estimated contamination from astrophysical backgrounds and point sources suggest that most of the emission is diffuse in nature.

(2) The observed absorption column density and temperature are consistent with those in the  $\eta$ Car region, suggesting the same origin as the diffuse X-ray emission in the vicinity of the Carina Nebula.

(3) Estimated physical properties of the plasma such as pressure, total energy, and mass can be explained by stellar winds from OB stars in the Carina Nebula or young SNR(s) with the age less than  $\sim 10^4$  yr. The SNR interpretation can provide the necessary energy and mass more easily.

(4) Absolute abundance values are strongly affected by abundances of metals fixed in spectral fits, allowing both the stellar-wind and SNR interpretations. The low nitrogen-to-oxygen and high iron-to-oxygen ratios derived from the spectral fits may support that the diffuse plasma heated up by stellar winds from main-sequence OB stars. The abundance ratios can be produced by a mixture of stellar winds and SNRs, as well.

The authors acknowledge discussion with Y. Hydo. K.H. is supported by the NASA Astrobiology Program under RTOP 344-53-51.

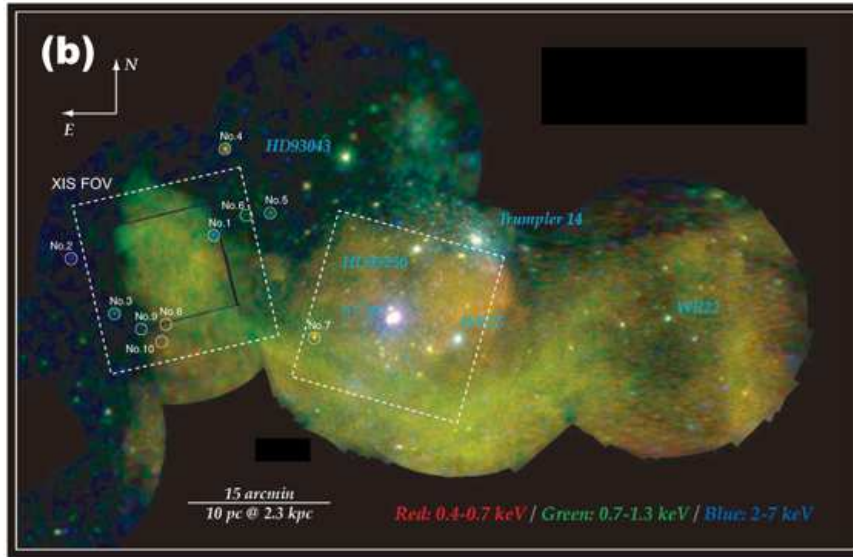
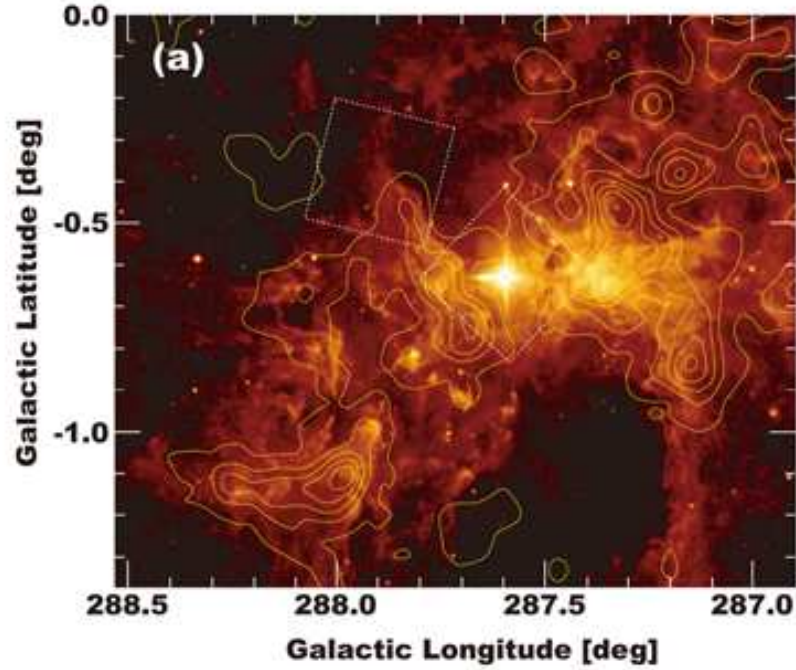


**Fig. 1.** (a) An MSX band-A  $8.28 \mu\text{m}$  image of the Carina nebula taken from the NASA/IPAC Infrared Science Archive. Yellow contours show the  $12\text{CO}$  ( $J=2-1$ ) map (Yonekura et al. 2005). Two white boxes represent field-of-views of this (upper left) and previous Suzaku observations (lower right, Hamaguchi et al. 2007). (b) An EPIC MOS mosaic of the same nebula with XMM-Newton taken from the XMM-Newton Image Gallery. The red, green and blue colors show soft ( $0.4\text{--}0.7 \text{ keV}$ ), medium ( $0.7\text{--}1.3 \text{ keV}$ ) and hard ( $2\text{--}7 \text{ keV}$ ) X-ray emission, respectively. Circles and numbers indicate point sources detected in our analysis (see §4).

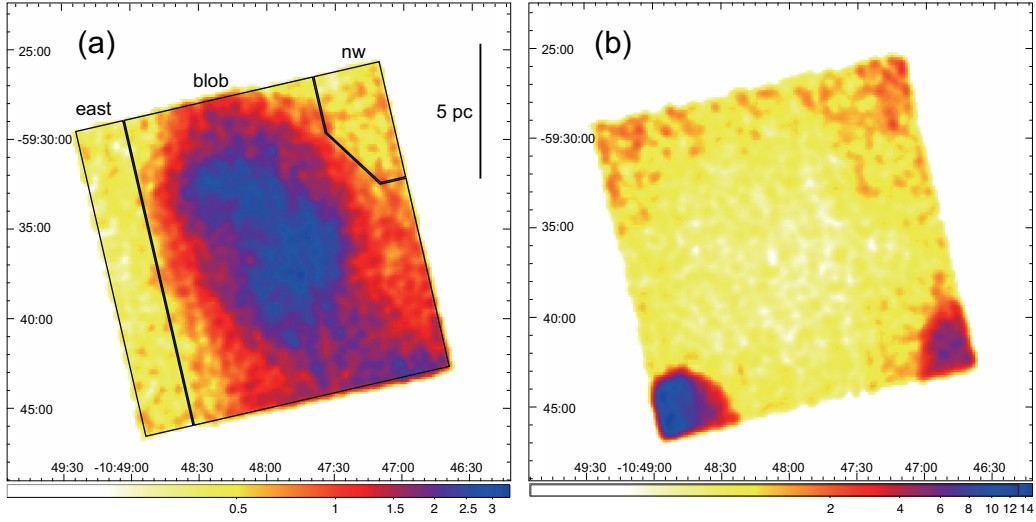


**Fig. 2.** Suzaku BI images of the eastern tip region of the Carina nebula in the (a) 0.2–2 keV and (b) 2–10 keV bands, displayed on the J2000.0 coordinates. For clarity, images are binned by a factor of 8 and smoothed by a Gaussian of  $\sigma = 3$  pixels. Vignettings are corrected (see §2). The unit of intensity in the greyscale wedge is arbitrary. Solid black lines mark regions utilized in the spectral analysis. The strong emission at the bottom-left and -right parts of the panel (b) corresponds to calibration  $^{55}\text{Fe}$  sources.

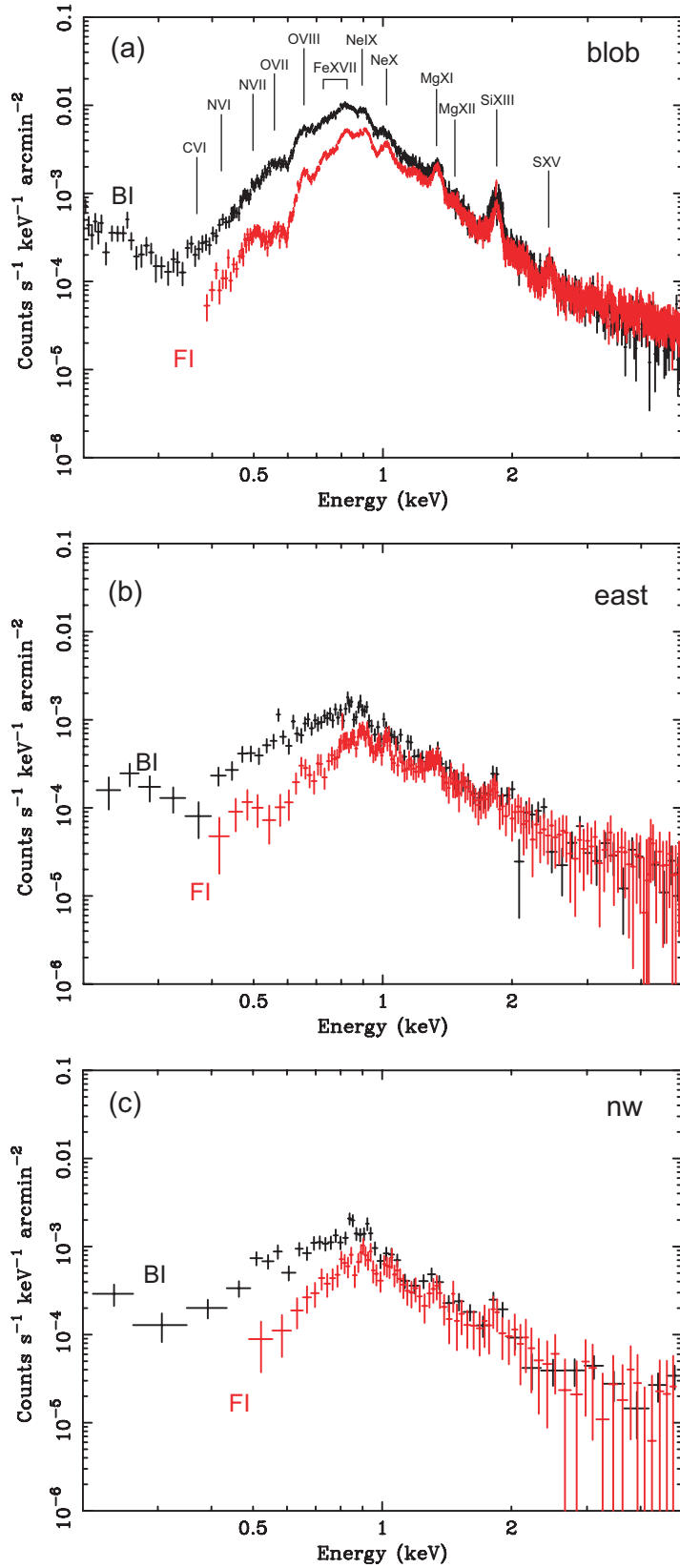


**Fig. 3.** Background-subtracted BI (black) and FI (red) spectra of (a) the blob, (b) the east, and (c) the nw regions. Center energies of emission lines are shown in the panel (a). For comparison, the vertical axis is normalized by the angular size of each region. 17

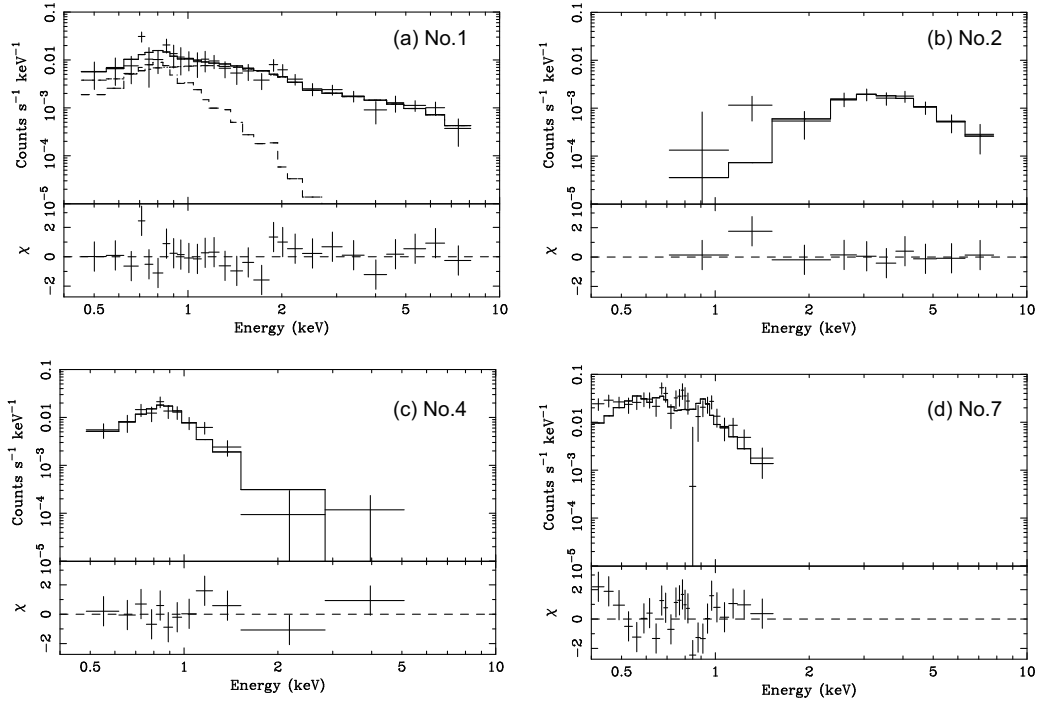


**Fig. 4.** XMM-Newton EPIC-pn spectra of the bright point sources (No.1, 2, 4, and 7). The solid lines show the best-fit absorbed plasma models. The dotted lines in the panel (a) show two plasma components. The bottom panels exhibit residuals from the best-fit models.

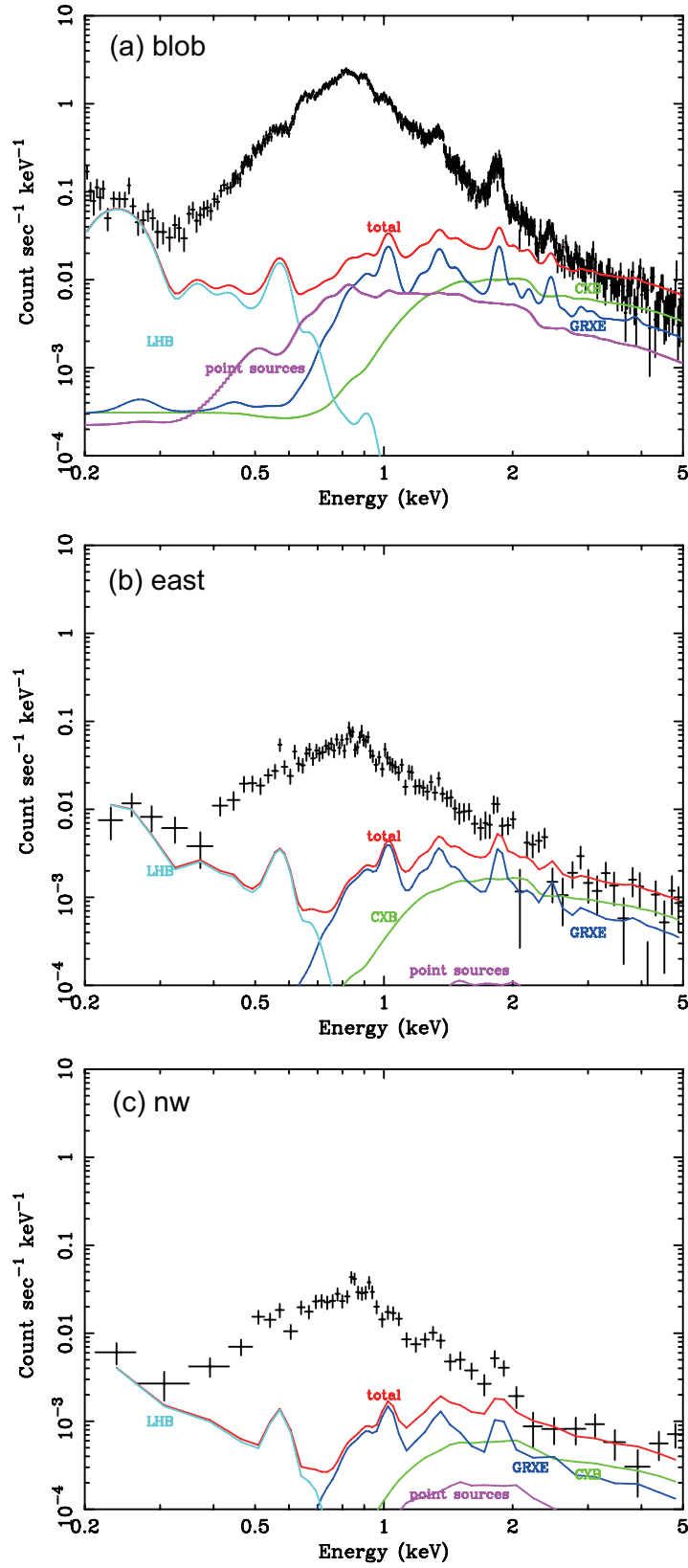
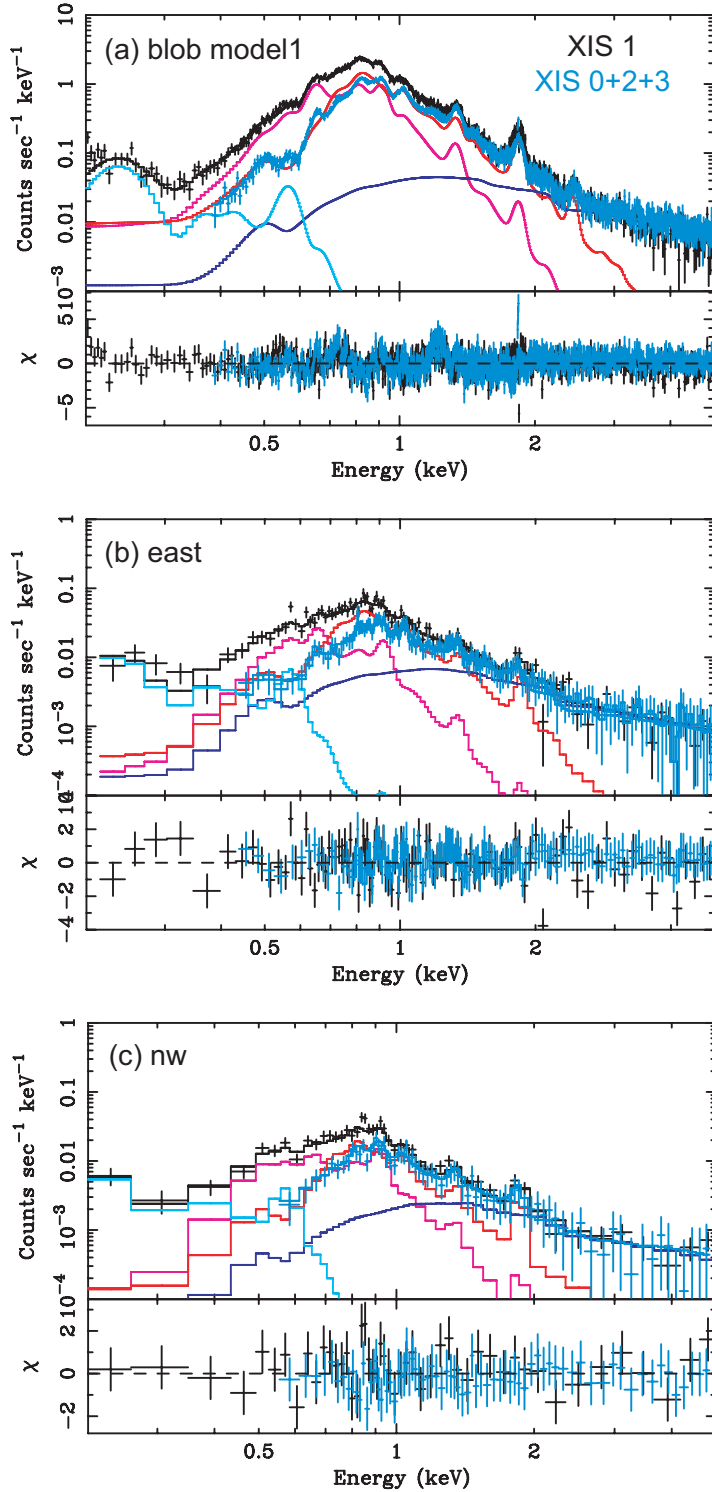
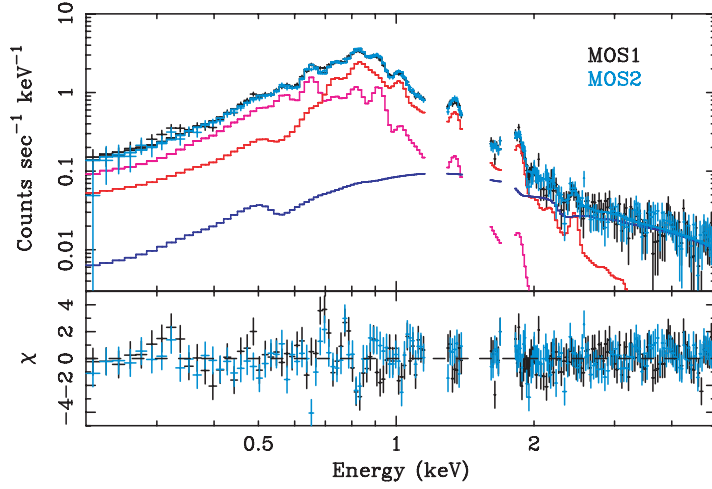


Fig. 5. Background-subtracted BI spectra of (a) the blob, (b) the east, and (c) the nw regions. Solid lines show estimated contamination from X-ray sources.



**Fig. 6.** Best-fit spectral results of the diffuse X-ray emission in (a) the blob, (b) the east, and (c) the nw regions. The best-fit model is shown in a solid black line. The model components for the XIS1 spectrum are shown in solid colored lines (cyan: the LHB component, magenta and red: the two-temperature plasma component, blue: the power-law component). See tables 3 and 4 for the obtained parameters.



**Fig. 7.** XMM-Newton MOS fitting result of the diffuse X-ray emission in the blob region. Line colors are the same as figure 6 but for the MOS1 and MOS2 data. See table 5 for the obtained parameters.

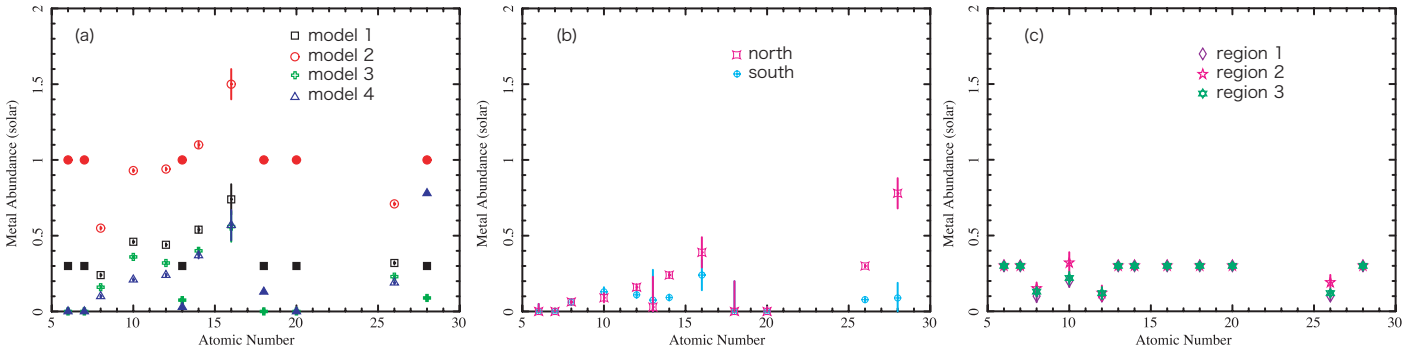


**Fig. 8.** Abundance distributions in (a) the blob region in the eastern tip region (this paper), (b) the north and south regions in the  $\eta$  Car region (Hamaguchi et al. 2007), and (c) sub-regions in M17 (Hyodo et al. 2008). The filled marks represent the fixed values.

**Table 1.** Properties of XMM-Newton point sources.

No.	R.A. <sup>a</sup>	Decl. <sup>a</sup>	$C_{\text{MOS}}^{\text{b}}$	$C_{\text{pn}}^{\text{b}}$	Flux <sup>c</sup>	Var <sup>d</sup>	Counterpart <sup>e</sup>
1	10:47:31.68	-59:32:33.7	199±13	411±30	3.8	No	2MASS J 10473148-5932345
2	10:49:28.08	-59:34:55.2	68±8	124±17	1.1	No	2MASS J 10492780-5935000
3 <sup>f</sup>	10:48:52.80	-59:40:39.4	62±9	22±13	0.07	Yes	2MASS J 10485248-5940392
4	10:47:22.80	-59:23:37.3	66±8	174±19	0.38	No	2MASS J 10472233-5923392
5	10:46:45.84	-59:30:13.0	30±7	83±15	0.27	No	2MASS J 10464595-5930130 GSC 0862602325
6	10:47:05.28	-59:30:27.0	15±7	61±17	0.20	No	2MASS J 10470505-5930247
7 <sup>g</sup>	10:46:09.12	-59:43:08.0	—	336±28	0.79	No	2MASS J 10460901-5943025
8	10:48:10.80	-59:41:44.9	47±10	73±22	0.23	No	2MASS J 10480990-5941489
9	10:48:30.96	-59:42:14.8	26±8	78±19	0.25	No	2MASS J 10483064-5942144
10	10:48:14.16	-59:43:32.2	15±9	81±19	0.26	No	—

<sup>a</sup> Source positions in J2000 coordinates.

<sup>b</sup> Background-subtracted photon counts detected with EPIC MOS and pn in 0.4–10 keV.  $C_{\text{MOS}}$  is the average counts of MOS1 and MOS2. Errors are  $1\sigma$ .

<sup>c</sup> The 0.4–10 keV X-ray flux in  $10^{-13}$  erg s<sup>-1</sup> cm<sup>-2</sup> which corresponds to  $6 \times 10^{31}$  erg s<sup>-1</sup> at 2.3 kpc. Fluxes of No.1, 2, 4, and 7 are derived from the spectral fittings, while the other are estimated from  $C_{\text{pn}}$  assuming the thin-thermal plasma model (see text).

<sup>d</sup> Time variability based on the  $\chi^2$  statistics.

<sup>e</sup> Counterpart candidates within 10 arcsec of the X-ray position, based on searches of the 2MASS and AGAST catalogs.

<sup>f</sup> This source falls in the CCD gap of pn.

<sup>g</sup> This source is outside the FOV of MOS.

**Table 2.** Results of the spectral fits to the point sources<sup>a</sup>.

No.	$N_{\text{H}}^{\text{b}}$	$kT^{\text{c}}$	Normalization <sup>d</sup>	$L_{\text{X}}^{\text{e}}$	$\chi^2/\text{d.o.f.}$
1	$0.17_{-0.12}^{+0.57}$	$0.42_{-0.18}^{+0.45}, > 32$	$4.8_{-2.9}^{+4.1} \times 10^{-5}, 2.5_{-0.6}^{+0.5} \times 10^{-4}$	3	19.5/25
2	$9.6_{-3.8}^{+6.3}$	$1.8_{-0.8}^{+2.3}$	$1.0 \pm 0.1 \times 10^{-3}$	6	3.5/7
4	$< 0.95$	$0.70_{-0.44}^{+0.10}$	$4.4 \pm 0.7 \times 10^{-5}$	0.3	7.1/9
7	$0.72_{-0.16}^{+0.17}$	$0.12_{-0.03}^{+0.04}$	$8.4_{-4.5}^{+4.6} \times 10^{-2}$	80	37.6/23

<sup>a</sup> A single plasma model is assumed for No. 2, 4, and 7, while a two temperature model is used for No.1. A metal abundance is fixed at 0.3 solar value. Errors refer to the 90% confidence range.

<sup>b</sup> Hydrogen column density in  $10^{22} \text{ cm}^{-2}$ .

<sup>c</sup> Plasma temperature in keV.

<sup>d</sup> Normalization factor of the APEC model, representing  $10^{-14}/4\pi D^2 EM$ , where  $D$  is a distance to the Carina nebula and  $EM$  is an emission measure in  $\text{cm}^{-3}$ .

<sup>e</sup> Absorption-corrected 0.4–10 keV luminosity in  $10^{32} \text{ erg s}^{-1}$  assuming a distance of 2.3 kpc.

**Table 3.** Results of the two-temperature plasma model fit to the diffuse X-ray emission in the blob region.

Model <sup>a</sup>	1	2	3	4	Typical error <sup>b</sup>
Two-temperature plasma component <sup>c</sup>					
$N_{\text{H}}$ ( $10^{22}$ cm <sup>-2</sup> )	0.23	0.25	0.22	0.26	0.01
$kT_1$ (keV)	0.25	0.24	0.25	0.24	0.01
$kT_2$ (keV)	0.55	0.56	0.55	0.54	0.01
C (solar)	0.3 (fixed)	1.0 (fixed)	0.0 (fixed)	0.0 (fixed)	–
N (solar)	0.3 (fixed)	1.0 (fixed)	0.0 (fixed)	0.0 (fixed)	–
O (solar)	0.24	0.55	0.16	0.10	0.01
Ne (solar)	0.46	0.93	0.36	0.21	0.01
Mg (solar)	0.44	0.94	0.32	0.24	0.01
Al (solar)	0.3 (fixed)	1.0 (fixed)	0.075 (fixed)	0.029 (fixed)	–
Si (solar)	0.54	1.1	0.40	0.37	0.02
S (solar)	0.74	1.5	0.56	0.57	0.1
Ar (solar)	0.3 (fixed)	1.0 (fixed)	0.0 (fixed)	0.13 (fixed)	–
Ca (solar)	0.3 (fixed)	1.0 (fixed)	0.0 (fixed)	0.0 (fixed)	–
Fe (solar)	0.32	0.71	0.23	0.19	0.01
Ni (solar)	0.3 (fixed)	1.0 (fixed)	0.089 (fixed)	0.78 (fixed)	–
$\log EM_1$ (cm <sup>-3</sup> arcmin <sup>-2</sup> )	54.9	54.6	55.0	55.4	0.02
$\log EM_2$ (cm <sup>-3</sup> arcmin <sup>-2</sup> )	54.5	54.2	54.6	54.7	0.02
Flux1 ( $10^{-14}$ erg s <sup>-1</sup> arcmin <sup>-2</sup> )	1.8	1.8	1.8	2.3	0.1
Flux2 ( $10^{-14}$ erg s <sup>-1</sup> arcmin <sup>-2</sup> )	2.2	2.2	2.2	1.8	0.1
Power-law component <sup>d</sup>					
Flux ( $10^{-14}$ erg s <sup>-1</sup> arcmin <sup>-2</sup> )	0.56	0.57	0.56	0.56	0.02
LHB component <sup>e</sup>					
Flux ( $10^{-14}$ erg s <sup>-1</sup> arcmin <sup>-2</sup> )	0.10	0.11	0.10	0.10	0.02
$\chi^2/\text{d.o.f.}$	1.24	1.31	1.21	1.22	
d.o.f.	1231	1231	1231	1231	

<sup>a</sup> Fitting models with different fixed abundances.

<sup>b</sup> Typical fitting errors at the 90% confidence level.

<sup>c</sup> A commonly-absorbed plasma model. Arabic numbers 1 and 2 denote the two temperature components. Parameter definitions are the same as those in table 2. Fluxes are calculated in 0.2–5 keV.

<sup>d</sup> A power-law model representing CXB, GRXE, and point sources. A photon index is fixed at 1.5. The same absorption for the two-temperature plasma is assumed. Normalization is photon keV<sup>-1</sup> cm<sup>-2</sup> at 1 keV.

<sup>e</sup> A single-temperature plasma model representing LHB. A plasma temperature is fixed at 0.1 keV.

**Table 4.** Results of the two-temperature plasma model fit to the diffuse X-ray emission in the east and nw regions<sup>a</sup>.

Region	east	nw
Two-temperature plasma component		
$N_{\text{H}}$ ( $10^{22}$ cm $^{-2}$ )	$0.21^{+0.09}_{-0.07}$	$0.32^{+0.11}_{-0.07}$
$kT_1$ (keV)	$0.20^{+0.04}_{-0.02}$	$0.19^{+0.02}_{-0.03}$
$kT_2$ (keV)	$0.54^{+0.04}_{-0.07}$	$0.41^{+0.10}_{-0.08}$
C (solar)	0.3 (fixed)	0.3 (fixed)
N (solar)	0.3 (fixed)	0.3 (fixed)
O (solar)	$0.15^{+0.12}_{-0.06}$	$0.07^{+0.04}_{-0.02}$
Ne (solar)	$0.33^{+0.31}_{-0.14}$	$0.27^{+0.14}_{-0.05}$
Mg (solar)	$0.30^{+0.29}_{-0.14}$	$0.25^{+0.16}_{-0.10}$
Al (solar)	0.3 (fixed)	0.3 (fixed)
Si (solar)	$0.43^{+0.37}_{-0.20}$	$0.96^{+0.57}_{-0.43}$
S (solar)	0.74 (fixed)	0.74 (fixed)
Ar (solar)	0.3 (fixed)	0.3 (fixed)
Ca (solar)	0.3 (fixed)	0.3 (fixed)
Fe (solar)	$0.16^{+0.10}_{-0.05}$	$0.17^{+0.03}_{-0.06}$
Ni (solar)	0.3 (fixed)	0.3 (fixed)
$\log EM_1$ (cm $^{-3}$ arcmin $^{-2}$ )	$54.3^{+0.4}_{-0.5}$	$55.0 \pm 0.7$
$\log EM_2$ (cm $^{-3}$ arcmin $^{-2}$ )	$54.0 \pm 0.2$	$54.3^{+0.8}_{-0.3}$
Flux1 ( $10^{-14}$ erg s $^{-1}$ arcmin $^{-2}$ )	$0.23^{+0.41}_{-0.15}$	$0.41 \pm 0.08$
Flux2 ( $10^{-14}$ erg s $^{-1}$ arcmin $^{-2}$ )	$0.48^{+0.31}_{-0.20}$	$0.45^{+0.11}_{-0.20}$
Power-law component		
Flux ( $10^{-14}$ erg s $^{-1}$ arcmin $^{-2}$ )	$0.56 \pm 0.06$	$0.55 \pm 0.09$
LHB component		
Flux ( $10^{-14}$ erg s $^{-1}$ arcmin $^{-2}$ )	$0.087^{+0.031}_{-0.032}$	$0.15^{+0.05}_{-0.06}$
$\chi^2/\text{d.o.f.}$	0.77	0.60
d.o.f.	245	111

<sup>a</sup> Notations and symbols are the same as table 3.

**Table 5.** Result of the two-temperature plasma model fit to the XMM MOS spectra of the blob region<sup>a</sup>.

Model	1
Two-temperature plasma component	
$N_{\text{H}}$ ( $10^{22}$ cm $^{-2}$ )	$0.19^{+0.03}_{-0.02}$
$kT_1$ (keV)	$0.24 \pm 0.01$
$kT_2$ (keV)	$0.58 \pm 0.01$
C (solar)	$1.2^{+0.4}_{-0.9}$
N (solar)	0.3 (fixed)
O (solar)	$0.23^{+0.02}_{-0.03}$
Ne (solar)	$0.44 \pm 0.07$
Mg (solar)	$0.46 \pm 0.07$
Al (solar)	0.3 (fixed)
Si (solar)	$0.48^{+0.07}_{-0.08}$
S (solar)	$0.48^{+0.20}_{-0.18}$
Ar (solar)	0.3 (fixed)
Ca (solar)	0.3 (fixed)
Fe (solar)	$0.32^{+0.05}_{-0.04}$
Ni (solar)	0.3 (fixed)
$\log EM_1$ (cm $^{-3}$ arcmin $^{-2}$ )	$54.8 \pm 0.1$
$\log EM_2$ (cm $^{-3}$ arcmin $^{-2}$ )	$54.5 \pm 0.1$
Flux1 ( $10^{-14}$ erg s $^{-1}$ arcmin $^{-2}$ )	$1.7 \pm 0.2$
Flux2 ( $10^{-14}$ erg s $^{-1}$ arcmin $^{-2}$ )	$2.7^{+0.2}_{-0.4}$
Power-law component	
Flux ( $10^{-14}$ erg s $^{-1}$ arcmin $^{-2}$ )	$0.84 \pm 0.05$
LHB component	
Flux ( $10^{-14}$ erg s $^{-1}$ arcmin $^{-2}$ )	$< 0.06$
$\chi^2/\text{d.o.f.}$	1.20
d.o.f.	337

<sup>a</sup> Notations and symbols are the same as table 3.

**Table 6.** Physical properties of the diffuse plasma in the blob region<sup>a</sup>.

Parameter	Scale Factor	$T_1$	$T_2$
Observed X-ray Properties			
$kT$ (keV)	–	0.3	0.6
$L_X$ (ergs s <sup>-1</sup> )	–	$2 \times 10^{34}$	$1 \times 10^{34}$
$V$ (cm <sup>3</sup> )	$\eta$	$1 \times 10^{57}$	$1 \times 10^{57}$
Estimated X-ray Plasma Properties			
$n_e$ (cm <sup>-3</sup> )	$\eta^{-1/2}$	0.3	0.4
$P/k$ (K cm <sup>-3</sup> )	$\eta^{-1/2}$	$2 \times 10^6$	$5 \times 10^6$
$U$ (ergs)	$\eta^{1/2}$	$4 \times 10^{47}$	$1 \times 10^{48}$
$t_{\text{cool}}$ (yr)	$\eta^{1/2}$	$1 \times 10^6$	$4 \times 10^6$
$M_{\text{plasma}}$ ( $M_\odot$ )	$\eta^{1/2}$	0.2	0.2

<sup>a</sup>  $\eta$  is a filling factor for the volume of the plasma.  $T_1$  and  $T_2$  indicate the two temperature plasma component in table 3 model 1.

## References

- Colombo, J.F.A., Mendez, M., & Morrell, N. I. 2003, MNRAS, 346, 704
- Cunha, K., & Lambert, D. L. 1994, ApJ, 426, 170
- Daflon, S., Cunha, A., & Butler, K. 2004, ApJ, 604, 326
- Davidson, K., Walborn, N. R., & Gull, T. R. 1982, ApJ, 254, L47
- Davidson, K., & Humphreys, R. M. 1997, ARA&A, 35, 1
- Dicky, J.M. , & Lockman, F.J. 1990, ARA&A, 28, 215
- Ebisawa, K., et al. 2005, ApJ, 635, 214
- Evans, N.R., Seward, F.D., Krauss, M.I., Isobe, T., Nichols, J., Schlegel, E.M., & Wolk, S.J. 2003, ApJ, 589, 509
- Ezoe, Y., Kokubun, M., Makishima, K., Sekimoto, Y., & Matsuzaki, K. 2006a, ApJ, 638, 860
- Ezoe, Y., Kokubun, M., Makishima, K., Sekimoto, Y., & Matsuzaki, K. 2006b, ApJ, 649, L123
- Feinstein, A. 1995, RMxAC, 2, 57
- Fukui, Y., Onishi, T., Abe, R., Kawamura, A., Tachihara, K., Yamaguchi, R., Mizuno, A., & Ogawa, H. 1999, PASJ, 51, 751
- Fujimoto, R., et al. 2007, PASJ, 59, 133
- Getman, K. V., et al. 2005, ApJS, 160, 319
- Güdel, M., Briggs, K. R., Montmerle, T., Audard, M., Rebull, L., & Skinner, S. L. 2008, Science, 319, 309
- Hamaguchi, K., et al. 2007, PASJ, 59, S151
- Harvey, P. M., Hoffmann, W. F., & Campbell, M. F. 1979, ApJ, 227, 114
- Huchtmeier, W. K., & Day G. A. 1975, A&A, 41, 153
- Hyodo, Y., Tsujimoto, M., Hamaguchi, K., Koyama, K., Kitamoto, S., Maeda, Y., Tsuboi, Y., & Ezoe, Y. 2008, PASJ, 60, 85
- Imanishi, K., Koyama, K., & Tsuboi, Y. 2001, ApJ, 557, 747
- Kelly, R., et al. 2007, PASJ, 59, S77
- Kokubun, M., et al. 2007, PASJ, 59, S53
- Koyama, K., Asaoka, I., Ushimaru, N., Yamauchi, S., & Corbert, R.H., 1990, ApJ, 362, 215
- Koyama, K., et al. 2007, PASJ, 59, S23
- McEntaffer, R. L., & Cash, W. 2008, ApJ, 680, 328
- Miyaji, T., Ishisaki, Y., Ogasaka, Y., Ueda, Y., Freyberg, M.J., Hasinger, G., & Tanaka, Y. 1998, å, 334, L13
- Mitsuda, K., et al. 2007, PASJ, 59, S1
- Moffat, A. F. J., et al. 2002, ApJ, 573, 191
- Serlemitsos, P. J., et al. 2007, PASJ, 59, S9
- Seward, F.D., Forman, W.R., Giacconi, R., Griffith, R.E., Harnden, F.R Jr., Jones, C., & Pye, J.P. 1979, ApJ, 234, L55
- Seward, F.D., & Chebowski, T. 1982, ApJ, 256, 530
- Smith, N., Egan, M. P., Carey, S., Price, S. D., Morse, P. J., & Price, P. A. 2000, ApJL, 532, L145
- Smith, R. K., Brickhouse, N. S., Liedahl, D. A., & Raymond, J. C. 2001, ApJL, 556, L91
- Smith, N. 2006, MNRAS, 367, 763

Smith, N., & Brooks, K. J. 2007, MNRAS, 379, 1279  
Snowden, S. L., Egger, R., Finkbeiner, D. P., Freyberg, M. J., & Plucinsky, P. P. 1998, ApJ, 493, 715  
Strüder, L., et al. (2001), A&A, 365, 18  
Takahashi, T., et al. 2007, PASJ, 59, S35  
Townsley, L. K., Feigelson, E. D., Montmerle, T., Broos, Patrick S., Chu, You-Hua., & Garmire, G. P. 2003, ApJ, 593, 874  
Tsuboi, Y., Koyama, K., Sakano, M., & Petre, R. 1997, PASJ, 49, 85  
Tsujiimoto, T., Nomoto, K., Yoshii, Y., Hashimoto. M., Yanagida. S., & Thielemann, F. -K. 1995, MNRAS, 277, 945  
Tsujiimoto, M., Hosokawa, T., Feigelson, E. D., Getman, K. V., & Broos, P. S. 2006, ApJ, 653, 409  
Tsujiimoto, M., Hyodo, Y., & Koyama, K. 2007, PASJ, 59, S229  
Turner, M.J.L., et al. å, 365, 27  
Yonekura, Y., et al. 2005, ApJ, 634, 476  
Yusef-Zadeh, F., Law, C., Wardle, M., Wang, Q. D., Fruscione, A., Lang, C. C., & Cotera, A. 2002, ApJ, 570, 665  
van der Hucht, K. A., Conti, P. S., Lundstrom, I., & Stenholm, B. 1981, Space Sci. Rev., 28, 227  
Wang, Q. D., Gotthelf, E. V., & Lang, C. C. 2002, Nature, 415, 148  
Weaver, R., McCray, R., Castor, R.J., Shapiro, P., & Moore, R. 1997, ApJ, 218, 377  
Willingale, R., Bleeker, J. A. M., van der Heyden, K. J., & Kaastra, J. S. 2003, å, 398, 1021  
Wolk, S. J., Bourke, T. L., Smith, R. K., Spitzbart, B., & Alves, J. 2002, ApJ, 850, L161